Journal of Power Sources 449 (2020) 227369

Contents lists available at ScienceDirect

Journal of Power Sources

journal homepage: www.elsevier.com/locate/jpowsour

Non-invasive yet separate investigation of anode/cathode degradation of lithium-ion batteries (nickel–cobalt–manganese vs. graphite) due to accelerated aging

Pouyan Shafiei Sabet [a,c,*], Alexander Johannes Warnecke [a,c], Frank Meier [a,c], Heiko Witzenhausen [a,c], Egoitz Martinez-Laserna [d], Dirk Uwe Sauer [a,b,c]

[a] Chair for Electrochemical Energy Conversion and Storage Systems, Institute for Power Electronics and Electrical Drives (ISEA), RWTH Aachen University, Jaegerstrasse 17/19, 52066, Aachen, Germany
[b] Institute for Power Generation and Storage Systems (PGS), E.ON ERC, RWTH Aachen University, Germany
[c] Juelich Aachen Research Alliance, JARA-Energy, Germany
[d] Ikerlan Technology Research Centre, Energy Storage and Management Area, P. J. M. Arizmendiarrieta, 2, 20500, Arrasate-Mondragon, Spain

HIGHLIGHTS

- Non-invasive yet separate investigation of anode and cathode degradation.
- Combining results from non-invasive and invasive investigations.
- Investigating calendric (700 days) and cyclic aging (3000 full cycle equivalents).

ARTICLE INFO

Keywords:
Lithium-ion battery
Nickel–manganese–cobalt
Electrochemical impedance spectroscopy
Battery aging

ABSTRACT

The non-invasive investigation of lithium-ion batteries is of great importance, e.g. for improvement of electrode materials or monitoring the state of health (SOH) in stationary or mobile applications. Electrochemical impedance spectroscopy (EIS) is a powerful tool for this task. Once the predominant processes in the impedance spectra are assigned to their corresponding electrode (i.e. anode or cathode), a tracking of both electrode's SOH becomes possible. In a previous work, this assignment has been performed. Two predominant processes were found: the impedance of the solid electroly interphase (SEI) and the NMC's charge transfer. In this work, this information is used for a non-invasive yet separate investigation of anode and cathode degradation throughout aging. Cells have been aged for about 700 days (calendric aging) or about 3000 full cycle equivalents (cyclic aging) at three different operating points each. A combination of impedance spectra analysis, differential voltage analysis (DVA) and post mortem analysis (PMA) determines the main aging mechanisms. Calendric aging: SEI-growth, CEI-growth, cathode-dissolution. Cyclic aging: anode's and cathode's particle-cracking, cathode-dissolution and possibly CEI-growth.

1. Introduction

This paper is based on our previous works [1,2]. Particularly in chapters 1 and 2 excerpts from these works are used.

The energy crisis is presumably the most severe issue that has to be faced. On the one hand, there are issues like decreasing fossil fuel reservoirs, global heating, CO_2-emissions or pollution in general. On the other hand, there is a steadily increasing energy demand. The severity of resulting consequences is also shown by substantial political decisions like the United Nations' Paris Agreement. At the same time, these consequences are increasingly becoming aware in society, e.g. expressed by movements like Fridays for Future.

Fortunately, there are strategies to overcome these issues; among these are for example the usage of renewable energy sources and pollution-free mobile solutions. In both fields, energy storage systems play an important role. Lithium-ion batteries (LIBs) are the most

* Corresponding author. Chair for Electrochemical Energy Conversion and Storage Systems, Institute for Power Electronics and Electrical Drives (ISEA), RWTH Aachen University, Jaegerstrasse 17/19, 52066, Aachen, Germany.
E-mail address: Pouyan.ShafieiSabet@isea.rwth-aachen.de (P. Shafiei Sabet).

https://doi.org/10.1016/j.jpowsour.2019.227369
Received 20 July 2019; Received in revised form 7 October 2019; Accepted 29 October 2019
Available online 18 December 2019
0378-7753/

promising battery technique due to their superior energy and power density [2,4,5]. State-of-the-art LIBs already provide satisfying energy/power densities [5–7] and aging behavior. However, these properties still have to be improved for further acceptance and market-penetration of environmentally aware energy systems. In this work, there is a focus of understanding state-of-the-art LIBs, comprising graphitic anodes and layered-oxide-cathodes.

Aging mechanisms of LIBs are very complex and influence each other [2]. Important aging mechanisms have been mentioned in our previous work [2]. For layered-oxide-cathodes, cation-mixing [8–12], cathode-dissolution [13–16], CEI-growth [7,17–20] and particle-cracking [21,22] have to be considered. The by far most important aging mechanism of graphitic anodes is formation and growth of SEI [23]. For cyclic aged cells, particle-cracking of graphitic anodes also becomes important [2,24,25].

To be able to investigate the complex interaction between these aging mechanisms, non-invasive measurement techniques are of special interest. EIS, which is such a technique, has the advantage of being simple and easy to implement, e.g. for battery management systems (BMS). However, the interpretation of the impedance spectra is non-trivial. One of the most important tasks is the assignment of the different processes in the impedance spectra to their corresponding electrode, i.e. to anode or cathode [2]. In our previous work [2], this task has been fulfilled for the cell-type, which is investigated in this work. In this work, the gained insights are utilized for a non-invasive yet separate investigation of anode and cathode degradation.

2. Experimental

A commercial LIB from Korean manufacturer EIG has been used for this study. It is of pouch-type, has a NMC(442)-cathode and a graphitic anode. The nominal capacity is 20 Ah, the nominal voltage is 3.65 V. The energy density is about 174 Wh kg^{-1} [2,26].

2.1. Investigation procedure

For a non-invasive yet separate investigation of anode/cathode degradation, the following procedure is performed.

1. In-depth investigation of impedance spectra, which has been performed in our previous work [2]. As a summary, impedance spectra of a pristine cell are depicted in Fig. 1 a). They are shifted in y-direction for visualization purposes. The corresponding distribution of relaxation times (DRT) in Fig. 1 b) shows that there are two predominant processes that have been assigned to the graphite's SEI-impedance and the NMC's charge transfer. The DRT is a mathematical transformation that takes an impedance spectrum as input argument and calculates the probability that a dominating process occurs at a specific frequency [1,2,27–30].
2. Calendric and cyclic aging at specified operating points, which are listed in Tables 1 and 2. These operating points are chosen to be orthogonal, so that for calendric aged cells, the influence of SOC (state of charge) and temperature can be investigated. For cyclic aged cells the influence of DOD (depth of discharge) and charge-current can be investigated.
3. Investigating changes in the impedance spectra throughout aging using the DRT and an equivalent circuit model (ECM). The ECM was developed by Witzenhausen [31] and mainly consists of one ohmic resistance that models the electrolyte (and other ohmic resistances), two HN-elements that model the SEI-impedance and the NMC's charge transfer, one Warburg-impedance that models the NMC's diffusion (graphite's diffusion is neglected) [1,2,31,32]. The regression process, using the DRT and the ECM, is explained in Section 2.2.
4. Performing a differential voltage analysis (DVA) and considering results from a former post mortem analysis (PMA) to gather further information about the origin of the changes in the impedance spectra.

2.2. Regression process

Fig. 2 shows the principle of the regression progress, exemplarily for a calendric aged cell, aged at 100% SOC and 35 °C. In Fig. 2 a), the evolution of the impedance spectra throughout aging is depicted. The impedance spectra are shifted in y-direction for visualization purposes. For a more a detailed investigation, the impedance spectra from the first and the last checkup are depicted separately in Fig. 2 b). Also plotted are the parts of the predominant processes in the impedance spectra, i.e. the SEI-impedance (blue line) and the NMC's charge transfer (red line). In the ECM, these processes are described by HN-elements [1,2,31,32]. Each HN-element is described by a time-constant τ and a resistance R. For the regression process, these time-constants are determined with high precision using the DRT. Thus, the number of variables in the regression process is minimized. The DRT (and the determined time-constants) for the two impedance spectra from Fig. 2 b) are depicted in Fig. 2 c) and d). The areas below the blue and red curves in

Table 1
Operating points of calendric aged cells. Storage time is about 700 days.

$SOC_{Storage}$ (%)	Temp. (°C)
100	35
80	35
80	45

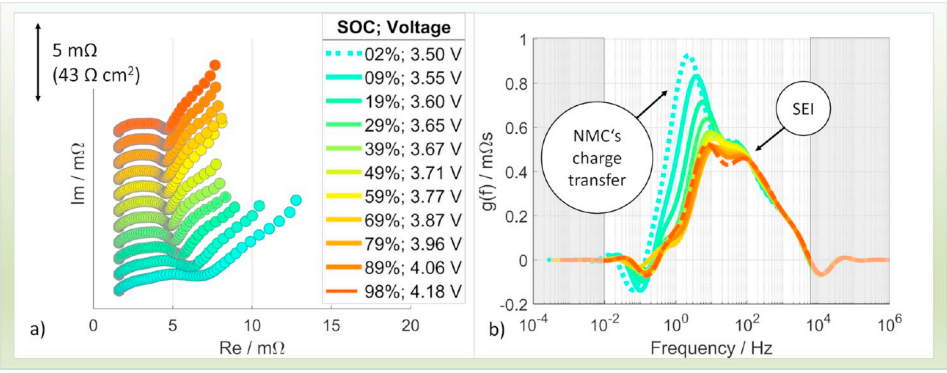

Fig. 1. a) Impedance spectra of a pristine cell from 0 to 100% SOC at 15 °C. b) Corresponding DRT. The assignment of the electrode processes has been performed in Ref. [2]. Reprinted from Ref. [2] with permission from Elsevier.

Table 2
Operating points of cyclic aged cells. Temperature is 25 °C. Full cycle equivalents are about 3000. Cha: charge current, Dch: discharge current.

SOC_{Middle} (%)	DOD (%)	Cha/Dch (C)
50	100	0.33/1
50	80	0.33/1
50	80	1/1

the DRT-plots represent the ohmic resistance of the corresponding process (i.e. SEI-impedance and NMC's charge transfer). As can be seen, the time-constants of the SEI-impedance decrease from the pristine to the aged state, whereas the time-constants of the NMC's charge transfer increase. On the other hand, the ohmic resistances of both processes increase. In the main part of this work, these findings as well other changes of the different ECM-parameters throughout aging are shown and discussed.

2.3. Checkup conditions

Periodically, a checkup has been performed for each cell. Calendric/cyclic aged cells have been tested approximately each three months/each 300 FCE (full cycle equivalents). The following values are shown and discussed:

- capacity (1C, discharge),
- impedance spectra at 50% SOC,
- pulse-resistance (1C, discharge, 10 s, 50% SOC),
- slow charge curves (C/5) for the DVA.

Capacity, pulse-resistance and slow charge curves are measured using a *Digatron MCT 10-06*-12 ME or *MCT 50-06-24*. Impedance spectra are measured in the frequency-range of 10 mHz to 6 kHz using a *Digatron EISmeter*. All checkups are performed at 25 °C using a *Binder MK53* or *CTS -40/550*.

2.4. Data handling

The quality of the impedance spectra have been checked using the free software *LinKK* [33], which is based on the Kramers-Kronig relations. This means, it is checked if the investigated cell can be regarded as an LTI-system (linear and time-invariant) at the moment of measuring its impedance spectrum. This is necessary for an investigation of impedance spectra with a linear equivalent circuit model (ECM). The time constants of the processes in the impedance spectra are determined using the open source software *FittingGUI* [34], which is based on the DRT. It has to be noticed that the results of the DRT are dependent on the DRT-parameters. However, these parameters have not been changed significantly for the several measurement sets in order to produce comparable results. Also, only results are shown after the DRT has converged [2]. Further, the plausibility of the determined DRT have been checked for specific impedance spectra (e.g. at begin of life and end of life) by using the free software *DRTTOOLS* [35]. All other data handling has been performed using *MathWorks Matlab* [1,2].

2.5. Post mortem analysis (PMA)

In 2017, Warnecke performed and published a PMA for this very cell type [26]. Several results of this PMA are used and connected to findings from the non-invasive investigations. Among these are results from the following measurements:

- ICP-OES (inductively coupled plasma optical emission spectrometry) to measure the lithium-content and NMC-content at the anode, and thus SEI-growth and cathode-dissolution,
- XRD (x-ray diffraction) to measure structural changes at the cathode, and thus cation-mixing,
- TGA (thermo-gravimetric analysis) to measure CEI-growth at the cathode.

Detailed information about experiments and evaluations of the PMA are found in Ref. [26].

3. Results and discussion

In the following, the calendric aged cells are referred to as $cell_{cal}$(-SOC, temperature). Analogously, the cyclic aged cells are referred to as

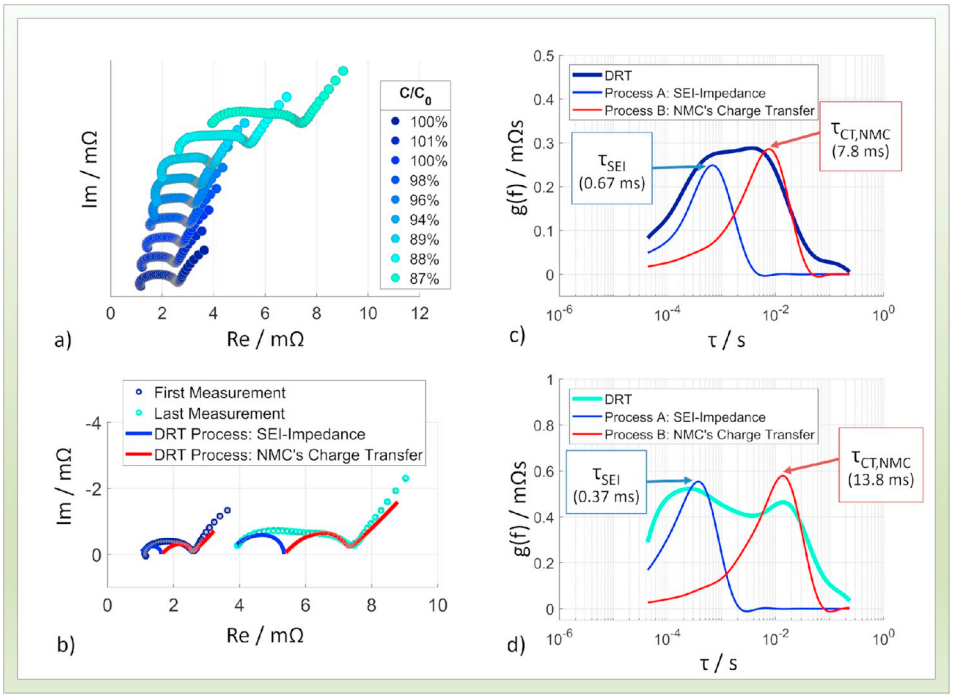

Fig. 2. a) Evolution of impedance spectra of a calendric aged cell at different SOH (impedance spectra are shifted in y-direction for visualization purposes). b) Impedance spectra at first and last checkup. c) and d) DRT of impedance spectra from first and last checkup to determine time-constants and resistances of SEI-impedance (blue line) and NMC's charge transfer (red line). (For interpretation of the references to colour in this figure legend, the reader is referred to the Web version of this article.)

$cell_{cyc}$(DOD, charge/discharge current). Furthermore, the condition that is assumed to lead to particularly fast aging is printed in bold.

For example, the calendric aged cell that is stored at 100% SOC and 35 °C is referred to as $cell_{cal}$(**100%**, 35 °C). 100% SOC is printed bold because it is expected to lead to faster aging than 80% SOC. Analogously, the cyclic aged cell that is cycled with 80% DOD and 1C/1C charge/discharge current is referred to as $cell_{cyc}$(80%, **1C**/1C). 1C is printed bold because it is expected to lead to faster aging than 0.33C. (The discharge-current is 1C for all cyclic aged cells.)

3.1. Capacity

Fig. 3 a) shows the normalized capacity of calendric aged cells over storage time and of cyclic aged cells over FCE. In the following figures, only the lower abscissa (and not the upper) is valid for calendric aged cells. Analogously, only the upper abscissa (and not the lower) is valid for cyclic aged cells.

For calendric aged cells, there is a great influence of the temperature in accordance to e.g. Ref. [36], presumably caused by an Arrhenius-dependency of the corresponding electrochemical reactions. $Cell_{cal}$(80%, **45** °C) shows a faster capacity-decrease than $cell_{cal}$(**100%**, 35 °C). As expected, $cell_{cal}$(80%, 35 °C) shows the slowest capacity-decrease of the calendric aged cells. Also visible is the influence of the DOD on cyclic aged cells. $Cell_{cyc}$(**100%**, 0.33C/1C) shows a faster capacity-decrease than the other cyclic aged cells. Surprisingly, $cell_{cyc}$(80%, 0.33C/1C) shows a slightly faster capacity-decrease than $cell_{cyc}$(80%, **1C**/1C), which is in contrast to literature results, e.g. Ref. [37]. The reasons of these findings are investigated in the following.

There is also another phenomenon that can be observed in Fig. 3 a). At the beginning of aging, approximately between 0 and 30 days (or between 0 and 100 FCE), the cell's capacities *in*crease. One possibility is an improved wetting of the electrodes by electrolyte. Another possibility is milling [38]. Milling (or particle-cracking) is a process that leads to a higher capacity due to cycling. Due to cycling, there is an increase of the electrodes' surfaces. For calendric aged cells, these cycling processes occur during the checkups. Both possibilities would lead to smaller impedances and thus increased capacities.

It has to be noticed that the capacity-increase cannot be explained by the overhang-effect in this case. The overhang is an effect that is potential-driven, has very high time constants and is able to explain a capacity-*in*crease for cells, which are discharged from a *higher* to a *lower* SOC. However, the cells in this work showed an SOC of about 68% when they were delivered [26]. Since the storage-SOCs are higher than 68% (i.e. 80% SOC and 100% SOC), the capacities are expected to *de*crease according to the overhang-effect. For further information about the overhang-effect it is referred to works of Lewerenz, e.g. Ref. [39].

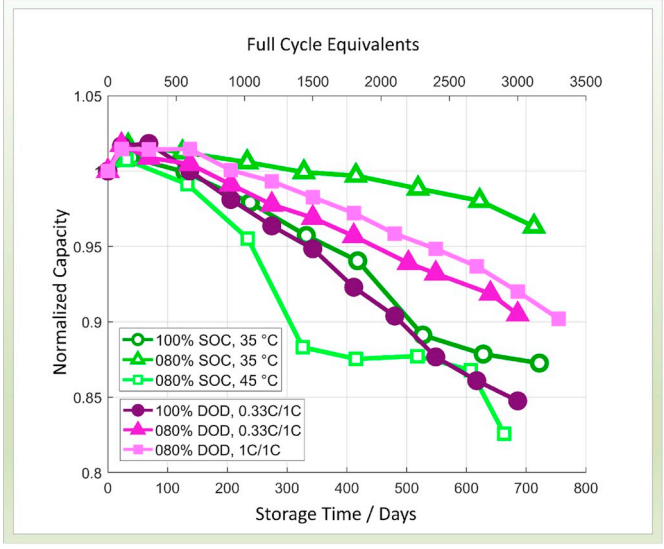

Fig. 3. Normalized capacity (1C discharge at 25 °C) for calendric and cyclic aged cells.

3.2. Analyzing impedance spectra

To analyze the impedance spectra, the corresponding DRT are calculated and the ECM from Witzenhausen [31] is used, as described in chapter 2.1. In the following, the values of the ECM-parameters that represent the predominant processes (SEI-impedance and NMC's charge transfer) are shown and discussed throughout aging.

Notice that e.g. Zhou et al. [40] investigate diffusion processes and find that these might have a high fraction of the overall impedance. However, in the following, diffusion processes are neglected because the focus lies on the separate investigation of anode and cathode degradation. To our knowledge, reliable (yet practical) methods for a distinction between anode and cathode diffusion are not available at the time being.

R_{SEI}: *Resistance of SEI-impedance*.The evolution of R_{SEI} throughout aging is shown in Fig. 4 a). The increase-factor of R_{SEI} is listed for all operating points in Table 3. It is defined as the quotient of R_{SEI} at the last and the second checkup. The second checkup (and not the first) has been chosen because the spread of R_{SEI} is lower at the second checkup (and the capacity-change is negligible). Note that for $cell_{cyc}$(80%, 0.33C/1C), the EIS-measurements of the first checkup are also used for the second checkup due to data loss.

R_{SEI} increases the most for calendric aged cells. Obviously, the temperature has a greater influence on R_{SEI} than the SOC, as mentioned, presumably caused by an Arrhenius-dependency of the corresponding electrochemical reactions. After about 700 days of storage, R_{SEI} has increased by a factor of about 5.1 for $cell_{cal}$(80%, **45** °C) and only by a factor of about 3.6 for $cell_{cal}$(**100%**, 35 °C). The change of R_{SEI} for $cell_{cal}$(80%, 35 °C) is negligible. Surprisingly, R_{SEI} of the cyclic aged cells does not increase, but decreases. The most significant decrease is by a factor of about 3.7 for $cell_{cyc}$(**100%**, 0.33C/1C) after about 2100 FCE, marked in Fig. 4 a) with "Minimum".

For calendric aged cells, the increase of R_{SEI} is assumed to be caused by SEI-growth, as depicted in the scheme in Fig. 5 a). For cyclic aged cells, the decrease of R_{SEI} is assumed to be caused by mechanical stress, which leads to particle-cracking. This leads to larger active surfaces and thus to decreased impedances, as depicted in the scheme in Fig. 5 b).

These assumptions are supported by the trends of R_{SEI}. $Cell_{cal}$(80%, **45** °C), which is expected to show the highest extent of SEI-growth, also shows the highest increase of R_{SEI}. Furthermore, in our previous work [2], microscopic and macroscopic pictures of the anode of a calendric aged cell (stored for about four years at 80% SOC, 35 °C) are shown and discussed. Clearly, an inhomogeneous deposition layer is visible that is assumed to be correlated to the SEI.

The increase-factors of R_{SEI} of the cyclic aged cells are close to each other. However, $cell_{cyc}$(**100%**, 0.33C/1C) seemingly shows the highest decrease of R_{SEI} throughout aging, presumably caused by the highest extent of particle-cracking.

τ_{SEI}: *Time constant of SEI-impedance.* The evolution of τ_{SEI} throughout aging is shown in Fig. 4 b). The corresponding increase-factor is listed in Table 4. Since τ_{SEI} decreases for all operating points, the decrease-factor = 1/increase-factor is also listed and discussed in the following.

τ_{SEI} decreases for both, calendric and cyclic aged cells with a clear trend. For calendric aged cells, the decrease-factor is the highest for $cell_{cal}$(80%, **45** °C). Again, the great influence of the temperature on the SEI is elucidated. For cyclic aged cells, the decrease-factor is the highest for $cell_{cyc}$(**100%**, 0.33C/1C), indicating the influence of the DOD.

As mentioned, although τ_{SEI} decreases for both, calendric and cyclic aged cells, it is assumed that the decrease has different reasons. This is explained as follows.

Calendric aging: according to the scheme in Fig. 5 a), calendric aging leads to SEI-growth, which leads to an increase of the SEI-thickness d_{SEI}.

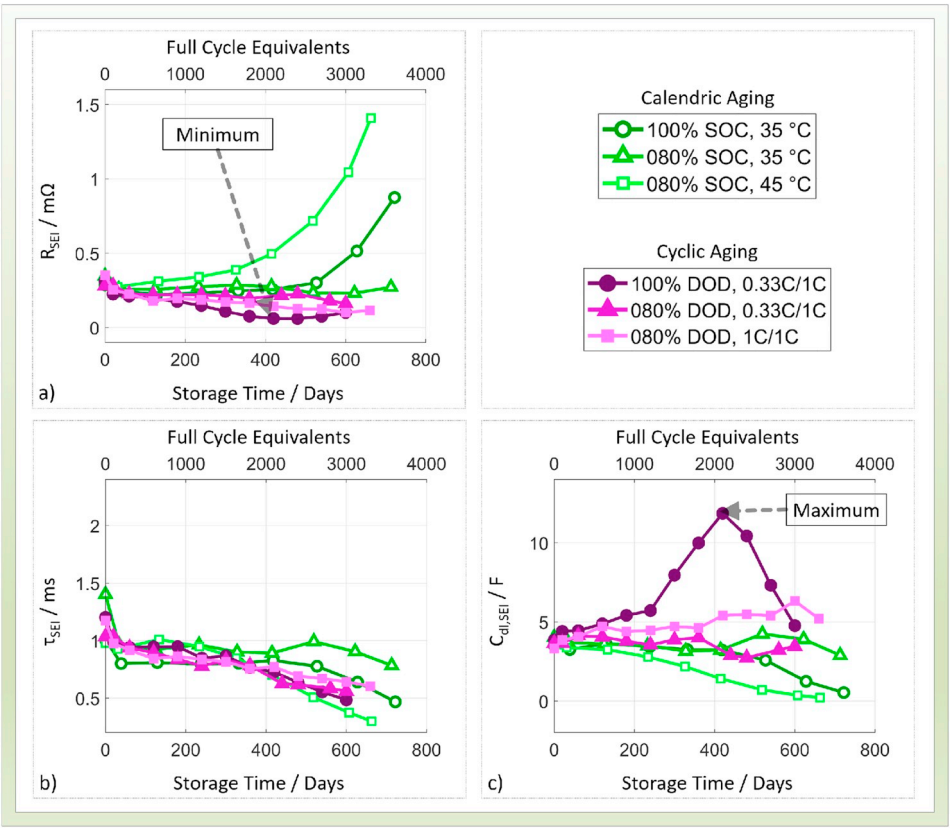

Fig. 4. a) R_{SEI}, b) τ_{SEI} and c) $C_{dl,SEI}$ for calendric and cyclic aged cells.

Table 3
Increase-factor of R_{SEI} in reference to second checkup.

Operating point	Increase-factor
100% SOC, 35 °C	3.55
80% SOC, 35 °C	1.05
80% SOC, 45 °C	5.14
100% DOD, 0.33C/1C	0.45
80% DOD, 0.33C/1C	0.57
80% DOD, 1C/1C	0.46

Table 4
Increase-factor and decrease-factor of τ_{SEI} in reference to second checkup.

Operating point	Increase-factor	Decrease-factor
100% SOC, 35 °C	0.58	1.71
80% SOC, 35 °C	0.81	1.23
80% SOC, 45 °C	0.32	3.09
100% DOD, 0.33C/1C	0.49	2.05
80% DOD, 0.33C/1C	0.54	1.85
80% DOD, 1C/1C	0.62	1.62

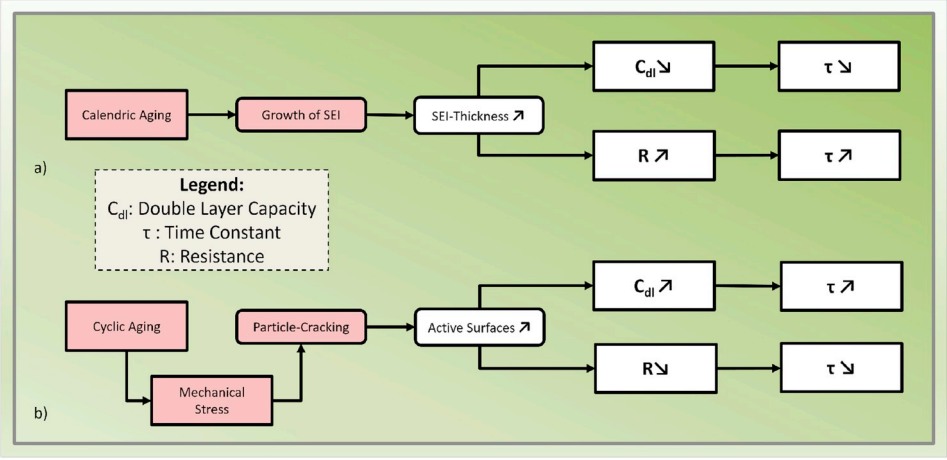

Fig. 5. Scheme of increasing/decreasing time constants of the SEI-impedance due to a) calendric and b) cyclic aging.

According to our previous work [2], this leads to a decrease of the SEI's double layer capacity $C_{dl,SEI}$ that is modeled as a simple capacitor, using the correlation

$$C_{dl,SEI} \propto A_{SEI} / d_{SEI}, \quad (1)$$

with A_{SEI} being the area of the SEI, which is assumed not to increase due to SEI-growth. For calendric aged cells, the decrease of $C_{dl,SEI}$ is seemingly more significant than the increase of R_{SEI}, leading, all in all, to a decrease of τ_{SEI} throughout aging, as shown in Fig. 4 b). This is due to the correlation

$$\tau_{SEI} = R_{SEI} \cdot C_{dl,SEI}. \quad (2)$$

Cyclic aging: according to the scheme in Fig. 5 b), cyclic aging leads to mechanical stress, which leads to particle-cracking and larger active surfaces (due to decreased particle-sizes). Eventually, this leads to a decrease of R_{SEI}, which is shown in Fig. 4 a). According to Equation (1), the larger active surfaces might also increase $C_{dl,SEI}$. This is shown in Fig. 4 c), particularly for cell$_{cyc}$(**100%**, 0.33C/1C) at about 2100 FCE, marked with "Maximum". For cyclic aged cells, the decrease of R_{SEI} is seemingly more significant than the increase of $C_{dl,SEI}$, leading, all in all, to a decrease of τ_{SEI}, as shown in Fig. 4 b) and according to Equation (2).

The trends of τ_{SEI} for both, calendric and cyclic aged cells support these assumptions. Cell$_{cal}$(80%, **45** °C), which is expected to show the highest extent of SEI-growth (which leads to a decrease of $C_{dl,SEI}$), also shows the highest decrease of τ_{SEI} of calendric aged cells. Further, cell$_{cyc}$(**100%**, 0.33C/1C), which is expected to show the highest extent of particle-cracking (which leads to a decrease of R_{SEI}), also shows the highest decrease of τ_{SEI} of cyclic aged cells.

$R_{CT,NMC}$: Resistance of NMC's Charge Transfer. The evolution of $R_{CT,NMC}$ throughout aging is shown in Fig. 6 a). The corresponding increase-factor is listed in Table 5.

$R_{CT,NMC}$ increases the most for cell$_{cal}$(80%, **45** °C). It also increases significantly for cell$_{cal}$(**100%**, 35 °C) and cell$_{cyc}$(**100%**, 0.33C/1C). The increase for other cells is negligible.

Table 5
Increase-factor for $R_{CT,NMC}$ in reference to third (sic!) checkup.

Operating point	Increase-factor
100% SOC, 35 °C	1.98
80% SOC, 35 °C	1.13
80% SOC, 45 °C	3.18
100% DOD, 0.33C/1C	2.62
80% DOD, 0.33C/1C	1.31
80% DOD, 1C/1C	1.17

Although $R_{CT,NMC}$ increases for both, calendric and cyclic aged cells, it is possible that the increase has different reasons.

In general, the aging of NMC might be caused by different reasons that have been mentioned in chapter 1. As a reminder, these are the following: cation-mixing, cathode-dissolution, CEI-growth and particle-cracking. Since there is an increase for both, cyclic and calendric aged cells, it is assumed that at least structural changes, CEI-growth and/or cathode-dissolution have occurred. This is because particle-cracking is expected to mainly occur in cyclic aged cells.

However, notice that Tsai et al. find that particle-cracking in NMC-particles might also occur at high voltages, i.e. in calendric aged cells [22]. They also find that particle-cracking in layered-oxide-cathodes leads to loss of mechanical and electrical contact within the particle, which leads to increased resistances [1,22]. Notice that this behavior is in contrast to that of the SEI's resistance, which is assumed to decrease due to particle-cracking, shown in the scheme in Fig. 5 b).

This means, particle-cracking is potentially a cause for the increased values of $R_{CT,NMC}$ of both, cyclic and calendric aged cells. However, the evaluation of $\tau_{CT,NMC}$ in the next paragraph will suggest that particle-cracking is indeed expected in cyclic aged cells but can be neglected

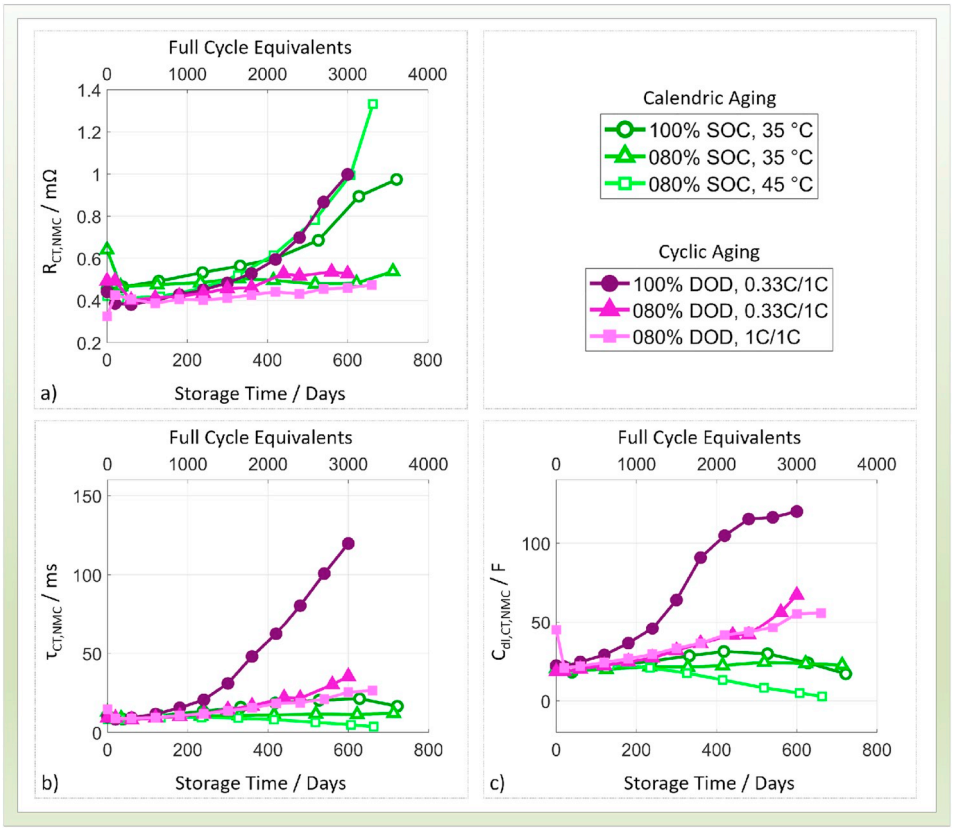

Fig. 6. a) $R_{CT,NMC}$, b) $\tau_{CT,NMC}$ and c) $C_{dl,CT,NMC}$ for calendric and cyclic aged cells.

Table 6
Increase-factor for $\tau_{CT,NMC}$ in reference to second checkup.

Operating point	Increase-factor
100% SOC, 35 °C	1.97
80% SOC, 35 °C	1.37
80% SOC, 45 °C	0.45
100% DOD, 0.33C/1C	14.4
80% DOD, 0.33C/1C	3.89
80% DOD, 1C/1C	2.98

Table 7
Increase-factor for R_{ser} in reference to second checkup.

Operating point	Increase-factor
100% SOC, 35 °C	3.53
80% SOC, 35 °C	1.39
80% SOC, 45 °C	4.34
100% DOD, 0.33C/1C	1.86
80% DOD, 0.33C/1C	1.36
80% DOD, 1C/1C	1.28

in calendric aged cells.

$\tau_{CT,NMC}$: Time constant of NMC's Charge Transfer. The evolution of $\tau_{CT,NMC}$ throughout aging is shown in Fig. 6 b). The corresponding increase-factor is listed in Table 6.

There is a clear trend for $\tau_{CT,NMC}$: each cyclic aged cell shows a higher increase-factor of $\tau_{CT,NMC}$ than each calendric aged cell. Cell$_{cyc}$(**100%**, 0.33C/1C) shows by far the highest increase of $\tau_{CT,NMC}$.

The increase of $\tau_{CT,NMC}$ of cyclic aged cells is assumed to be caused by particle-cracking. This assumption is supported by the increasing values of $C_{dl,CT,NMC}$ for cyclic aged cells, as shown in Fig. 6 c). This is due to increased active surfaces. The NMC's volume expansion during lithiation/delithiation is expected to have a high impact on the severity of the cathode's particle-cracking. In a PMA [26], it is measured to about 1.7% [26], in good accordance to literature values of about 1–2%, e.g. Ref. [11]. Notice that the NMC's volume expansion is small in comparison to that of e.g. graphite, which is about 10% [3]. Still, even these small volume expansions seemingly lead to significant particle-cracking.

As mentioned in the previous paragraph, particle-cracking is assumed to be negligible for calendric aged cells. This is because of the following: if particle-cracking would occur in calendric aged cells, the values of $C_{dl,CT,NMC}$ are expected to increase due to larger active surfaces. However, as shown in Fig. 6 c), this is not generally the case for calendric aged cells.

R_{ser}: Mainly Electrolyte Resistance. R_{ser} represents mainly the electrolyte-resistance, but also the resistances of the separator and the current-collectors [1,2]. Its evolution throughout aging is shown in Fig. 7 a). The corresponding increase-factor is listed in Table 7.

R_{ser} increases the most for cell$_{cal}$(80%, **45** °C), in qualitative accordance to results from literature, e.g. Ref. [41]. Again, the strong influence of the temperature is emphasized. It also increases significantly for cell$_{cal}$(**100%**, 35 °C) and cell$_{cyc}$(**100%**, 0.33C/1C). The increase for the other cells is negligible.

Since R_{ser} is correlated to the electrolyte-resistance, it is also correlated to SEI-growth. This is because SEI is formed out of electrolyte-parts and lithium, leading to species like Li_2CO_3 [42]. Indeed, for calendric aged cells, the increase-factors of R_{ser} and R_{SEI} show the same trend. For cyclic aged cells, a different trend is noticed. Cell$_{cyc}$(**100%**, 0.33C/1C) shows the highest value of R_{ser}, in qualitative accordance to results from literature, e.g. Ref. [37]. However, it also shows relative low values of R_{SEI}. It is assumed that due to cycling, SEI is formed, destroyed, formed again, destroyed again, etc. This behavior is also explained in Ref. [43]. This process leads to a continuous loss of electrolyte and active lithium but not to SEI-growth and thus not to an increase of R_{SEI}.

3.3. Differential voltage analysis (DVA)

Fig. 8 shows the DVA in the last aging state of each cell. However, for cell$_{cyc}$(80%, 0.33C/1C), the DVA in the second to last aging state is shown (due to data loss). The DVA are shifted in y-direction for visualization purposes.

The cells that show severe degradation in the impedance spectra, i.e. cell$_{cal}$(80%, **45** °C), cell$_{cal}$(**100%**, 35 °C) and cell$_{cyc}$(**100%**, 0.33C/1C), have lost their distinct peaks in the DVA. For the other cells, these peaks are still (vaguely) visible.

The vanishing distinctness of peaks indicates decreasing homogeneities of graphite particles [39,44]. For calendric aged cells, the decrease of homogeneity is expected to be caused by passivation layers, e.g. SEI. As mentioned in chapter 3.2, macroscopic and microscopic images of a calendric aged anode sheet are depicted in our previous work [2]. This sheet shows passivation layers, which are indeed inhomogeneously distributed. It is assumed that the inhomogeneous distribution is caused by different pressures at the middle and the borders of the cells (since the cell is of pouch-type). Since the passivation layers cause higher resistances, their inhomogeneous distribution leads to locally different resistances. Thus, the graphite particles cannot be lithiated (or delithiated) simultaneously (i.e. uniformly). This leads to blurry or missing peaks in the DVA [39,44].

Cyclic aged cells do not seem to show a significant SEI-growth since their values of R_{SEI} decrease. However, the distinctness of their peaks also vanishes. This might be caused by an inhomogeneous current distribution, caused by inhomogeneous particle sizes (caused by particle-cracking at the anode). Furthermore, a continuous formation and

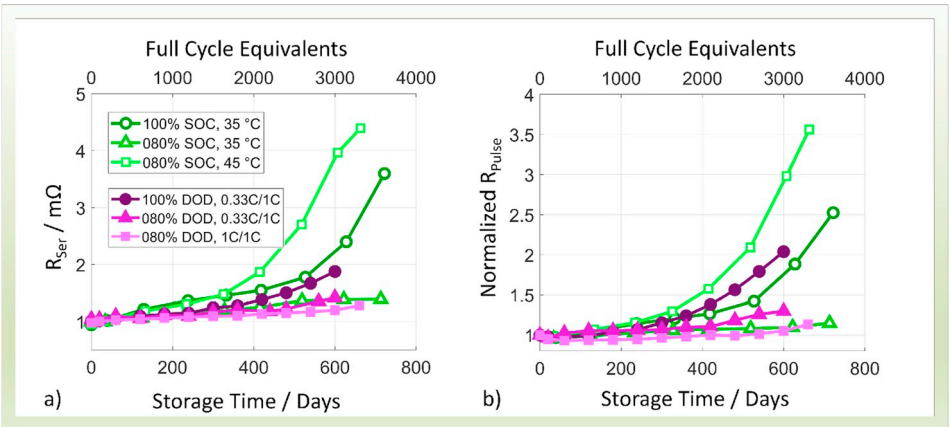

Fig. 7. a) R_{ser} and b) R_{Pulse} for calendric and cyclic aged cells. Notice: cell$_{cyc}$(80%, 0.33C/1C) showed an outlier of R_{Pulse} at 1200 FCE, which has been removed.

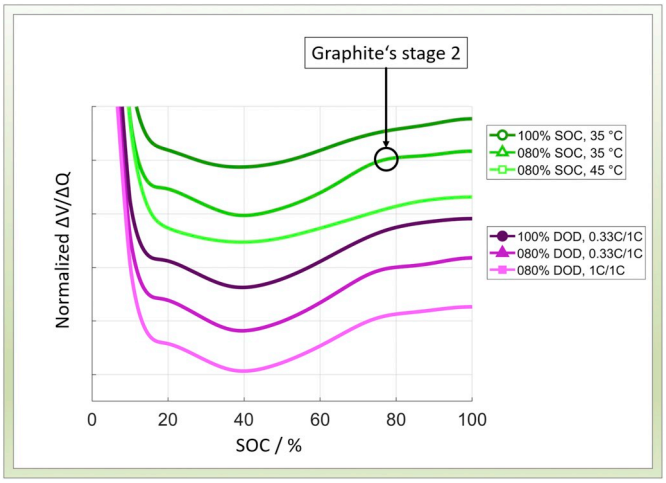

Fig. 8. DVA in the last aging state of each cell except $cell_{cyc}$(80%, 0.33C/1C), for which the DVA in the second to last aging state is shown.

destruction of SEI due to particle-cracking might enhance an inhomogeneous resistance-distribution. Once again, the graphite particles cannot be lithiated (or delithiated) simultaneously.

3.4. Summary of investigation of ECM-parameters

In Table 8, the assumed aging-mechanisms of anode and cathode as well as their possible origins are summarized. These results have been found by merely using non-invasive techniques (EIS and DVA). These aging mechanisms are assumed to be the following: SEI-growth (calendric aged anodes), particle-cracking (cyclic aged anodes) as well as CEI-growth and/or cathode-dissolution and/or cation-mixing (calendric and cyclic aged cathodes). Additionally, there is particle-cracking (cyclic aged cathodes). In the following, the non-invasive investigation is complemented by a PMA.

3.5. Post Mortem Analysis (PMA)

This chapter is based on works of Warnecke [26]; results from a PMA are shown, which was performed and published for this very cell-type in 2017. It is checked if the results from the PMA are in accordance to those found by EIS and DVA. And further, if they can determine the main aging-mechanism(s) of the cathode since there are different options. The aging mechanisms from Table 8 are investigated by means of PMA by the following measurements.

Lithium-content at Anode. The lithium content has been measured at the anode by means of ICP-OES and is listed in Table 9.

The lithium content is an indicator for SEI-growth because the SEI mainly consists of lithium and electrolyte-parts; SEI-compounds are for example Li_2CO_3 [42]. Since SEI-growth is assumed to be the main anode aging mechanism for calendric aged cells, it is expected that the highest lithium-contents are found for calendric aged cells. Indeed, the results from Table 9 show that the most lithium is found for $cell_{cal}$(80%, **45** °C) and $cell_{cal}$(**100%**, 35 °C). These are also the cells that show the highest increase-factors for R_{SEI}.

$Cell_{cyc}$(**100%**, 0.33C/1C) also shows an increased lithium-content. However, it shows decreased values of R_{SEI}. As explained in Section 3.2, this is assumed to be caused by continuous formation and destruction of SEI [43], leading to loss of active lithium and electrolyte without increasing R_{SEI}. As expected from the increase-factors of R_{SEI}, the other calendric and cyclic aged cells have less lithium-content, indicating less SEI-growth.

NMC-content at Anode. The NMC-content has also been measured by means of ICP-OES at the anode (and not at the cathode) because the sensitivity to detect concentration-changes is higher at the anode than at the cathode [26].

The NMC-content at the anode is listed in Table 9 and is an indicator for cathode-dissolution [26]. This is one of the possible reasons for cathode-degradation of both, calendric and cyclic aged cells. It is expected to have mainly an influence on $R_{CT,NMC}$ and $\tau_{CT,NMC}$. Indeed, cells that show the highest NMC-content at the anode also show the highest increase of $R_{CT,NMC}$, namely $cell_{cal}$(80%, **45** °C), $cell_{cal}$(**100%**, 35 °C) and $cell_{cyc}$(**100%**, 0.33C/1C). Thus, cathode-dissolution presumably leads to an impedance-increase of the cathode, in accordance to literature, e.g. Ref. [23].

It has to be noticed that the NMC-content has the same trend as the lithium content; thus, they are seemingly correlated. It is assumed that the NMC-content damages the SEI, which leads to SEI-breakdown and eventually to new SEI-formation, as known from literature, e.g. Ref. [23]. Gilbert et al. find that each manganese-atom at the SEI leads to a consumption of 95 lithium-atoms [15].

$\tau_{CT,NMC}$ shows by far the highest increase for $cell_{cyc}$(**100%**, 0.33C/1C), indicating the strong influence of the DOD. However, its NMC-content at the anode is lower than those of the calendric aged cells. This means that the increase of $\tau_{CT,NMC}$ in cyclic aged cells is not mainly

Table 8
Behavior of ECM-parameters throughout calendric and cyclic aging and possible reasons for this behavior.

ECM-	Calendric aging		Cyclic aging	
param.	Behavior	Assumption	Behavior	Assumption
R_{ser}	↗	Loss of active lithium and electrolyte due to SEI-growth	↗	Loss of active lithium and electrolyte due to continuous formation and breakdown of SEI due to particle-cracking at anode
R_{SEI}	↗	SEI-growth	↙	Increase of active surfaces of anode-particles due to particle-cracking at anode
τ_{SEI}	↙	Decrease of $C_{dl,SEI}$ due to SEI-growth	↙	R_{SEI} decreases due to particle-cracking at anode
$R_{CT,NMC}$	↗	CEI-growth and/or cathode-dissolution and/or cation-mixing	↗	CEI-growth and/or cathode-dissolution and/or cation-mixing and/or particle-cracking
$\tau_{CT,NMC}$	≈	$C_{dl,CT,NMC}$ stays approx. same or decreases (i.e. active surfaces of cathode-particles do not increase); particle-cracking can be neglected	↗	Increase of $C_{dl,CT,NMC}$ due to increase of active surfaces of cathode-particles due to particle-cracking at cathode (especially at high DOD)

Table 9
Lithium content and NMC-content measured by ICP-OES in Ref. [26] at about 700 days of storage time or 3000 FCE. Values marked by a star have been linearly extrapolated to the last checkup.

Operating point	Li (%)	NMC (%·10^{-3})
100% SOC, 35 °C	13	1.4
80% SOC, 35 °C	8	0.9
80% SOC, 45 °C	18	1.5
100% DOD, 0.33C/1C	12	1.0
80% DOD, 0.33C/1C	10*	0.7*
80% DOD, 1C/1C	N/A	N/A

caused by cathode-dissolution and must have different reasons. As discussed in chapter 3.2, particle-cracking is expected in cyclic aged cells. Thus, it is presumably the main cause of the increasing values of $R_{CT,NMC}$ and $\tau_{CT,NMC}$ in cyclic aged cells. Notice that particle-cracking has not been investigated explicitly in the PMA.

Structural Changes of NMC. Structural changes are correlated to restructuring of lithium and transition metals inside the cathode [26,45,46]. This might lead to cation-mixing and is investigated by XRD of the cathode-material. However, only two operating points have been investigated in detail in Ref. [26]. The corresponding cells are cell$_{cal}$(**100%**, 35 °C) and cell$_{cyc}$(80%, **1C**/1C). XRD have been measured at different C/C_0:

- $C/C_0 \approx$ 100%, 98%, 87%, 79% for cell$_{cal}$(**100%**, 35 °C)
- $C/C_0 \approx$ 100%, 90%, 54% for cell$_{cyc}$(80%, **1C**/1C)

Only for cell$_{cyc}$(80%, **1C**/1C) at $C/C_0 \approx$ 54% changes in the diffractogramm were found, indicating higher c/(a · b) values and thus structural changes. (a = b and c are the lattice parameters of NMC.) Thus, it can be concluded, that cation-mixing and structural changes are of minor importance for calendric aged cells and mainly occur due to severe cyclic aging.

Cathode Electrolyte Interphase (CEI). The CEI is investigated by TGA. Cathode material is heated and the corresponding weight-change Δm_{TGA} is measured. The higher the value of Δm_{TGA}, the higher the CEI-growth [26]. Table 10 lists the values of Δm_{TGA}. Only calendric aged cells have been investigated in Ref. [26].

The results of the TGA are as expected. Cell$_{cal}$(80%, **45** °C) shows the highest value of Δm_{TGA}, indicating the most CEI-growth. Cell$_{cal}$(**100%**, 35 °C) shows a lower value. Cell$_{cal}$(80%, 35 °C) shows a negligible value. It is assumed that CEI-growth leads to increased impedances at the cathode (increase of $R_{CT,NMC}$). The increase-factor of $R_{CT,NMC}$ is also listed in Table 10. For an easier comparison, normalized values, in reference to cell$_{cal}$(**100%**, 35 °C), are listed in brackets.

As can be seen, the qualitative results from both measurements are in accordance. The quantitative results differ slightly from each other, especially for cell$_{cal}$(80%, 35 °C). All in all, the results from the TGA support the assumption that the increase of $R_{CT,NMC}$ in calendric aged cells is additionally (or mainly) caused by CEI-growth.

3.6. Correlation of pulse-resistance to EIS-resistances

Along with the capacity, another important cell-property is the (normalized) pulse-resistance R_{Pulse}, which is shown in Fig. 7 b). In practice, the pulse-resistance's determination may not be suitable because the battery has to be charged/discharged with relative high currents. Therefore, its correlation to the different EIS-parameters (R_{ser}, R_{SEI}, $R_{CT,NMC}$) is a useful information, e.g. in (future) BMS. To investigate this issue, a correlation analysis based on Pearson has been performed. The correlation coefficients (CC) are in the range [-1, 1]. A value of −1 means there is perfect negative correlation. A value of 0 means there is no correlation, A value of 1 means there is perfect positive correlation. Table 11 shows the CC.

For both, calendric and cyclic aged cells, R_{Pulse} shows a high correlation to R_{ser} ($CC_{mean} = 0.94$). Since the correlation to R_{SEI} is positive for calendric aged cells, but negative for cyclic aged cells, the correlation to R_{SEI} is very small ($CC_{mean} = 0.12$). The correlation to $R_{CT,NMC}$ is slightly smaller ($CC_{mean} = 0.84$) than the correlation to R_{ser}.

The highest correlation is to $R_{CT,NMC}$, but only for calendric aged cells. Therefore, best practice is to investigate R_{Pulse} by investigating R_{ser}. This is also advantageous, because i) R_{ser} is measured at relative high frequencies, leading to low measurement durations and ii) R_{ser} corresponds in first proximity to the intersection of the impedance spectrum with the abscissa, i.e. it is easy and accurate to determine (no DRT or ECM is needed).

For the cells used in this study, there is also a strong correlation between R_{Pulse} and the capacity (from Fig. 3). This means, R_{ser} is suitable as an SOH-indicator in this case. Of course, for cell-types with a weak correlation between R_{Pulse} and the capacity, this is not the case.

Table 10
Increase-factor of $R_{CT,NMC}$ and Δm_{TGA} measured by TGA in Ref. [26] at about 700 days of storage time. Normalized values, in reference to cell$_{cal}$(**100%**, 35 °C), are listed in brackets.

Operating point	Increase-factor $R_{CT,NMC}$ (norm.)	Δm_{TGA} (%) (norm.)
100% SOC, 35 °C	1.98 (1.00)	1.1 (1.00)
80% SOC, 35 °C	1.13 (0.66)	0.2 (0.18)
80% SOC, 45 °C	3.18 (1.66)	1.3 (1.18)

Table 11
Pearson correlation coefficients (CC) to investigate the correlation between R_{Pulse} and the different EIS-resistances (R_{ser}, R_{SEI}, $R_{CT,NMC}$).

Operating point	CC(R_{ser})	CC(R_{SEI})	CC($R_{CT,NMC}$)
100% SOC, 35 °C	1.00	0.96	0.97
80% SOC, 35 °C	0.89	0.76	0.90
80% SOC, 45 °C	0.97	0.92	1.00
100% DOD, 0.33C/1C	0.99	−0.67	1.00
80% DOD, 0.33C/1C	0.97	−0.83	0.60
80% DOD, 1C/1C	0.83	−0.45	0.55
Mean (cal. and cyc.)	0.94	0.12	0.84
Mean (calendric)	0.95	0.88	0.96
Mean (cyclic)	0.93	−0.65	0.72

4. Conclusion

In a previous work [2], the predominant processes in the cell's impedance spectra of a lithium-ion battery (graphite vs. NMC) have been determined; these are the SEI-impedance and the NMC's charge transfer.

In this work, the insights from Ref. [2] are utilized for a non-invasive yet separate investigation of anode and cathode degradation of a lithium-ion battery (graphite vs. NMC). For this purpose, cells have been aged at different operating points. Evaluating the non-invasive investigations, the main aging mechanisms have been concluded to the following. SEI-growth (calendric aged anodes), particle-cracking (cyclic aged anodes) as well as CEI-growth and/or cathode-dissolution and/or cation-mixing (calendric and cyclic aged cathodes). Additionally, there is particle-cracking (cyclic aged cathodes).

Results from a PMA, which was performed in 2017 [26], complemented the non-invasive investigations. The PMA restricted the possible origins of the cathode's aging mechanisms to the following. Calendric aging: CEI-growth and cathode-dissolution. Cyclic aging: Mainly particle-cracking, also cathode-dissolution. CEI-growth cannot be excluded since it was not investigated for cyclic aged cells in the PMA.

Additionally, a correlation analysis (based on Pearson) has been performed for the pulse-resistance and the different resistances from the impedance spectra. It was found that there is a high correlation between the pulse-resistance and the ohmic resistance of the impedance spectrum. This information might be particularly useful for SOH-algorithms in BMS.

The non-invasive yet separate investigation of anode and cathode degradation has high potential for improvements of battery systems. Weaknesses of state of the art anodes and cathodes can specifically be investigated, leading eventually to improved electrode materials. More reliable algorithms for BMS can be developed, which take the SOH of both electrodes into account. Also, improved strategies for stationary battery systems might be developed. For example, it was found that an increased charge-current might be advantageous since it leads to

particle-cracking at the anode and thus to decreased impedances of the SEI.

Declaration of competing interest

The authors declare that they have no known competing financial interests or personal relationships that could have appeared to influence the work reported in this paper.

Acknowledgment

This work originated within the project *Batteries2020* (GC. NMP. 2013–1 Grant. 608936). The authors would like to thank the "European Union's Seventh Programme for Research, Technological Development and Demonstration".

References

[1] P. Shafiei Sabet, G. Stahl, D.U. Sauer, Non-invasive investigation of predominant processes in the impedance spectra of high energy lithium-ion batteries with Nickel-Cobalt-Aluminum cathodes, J. Power Sources 406 (2018) 185–193.
[2] P. Shafiei Sabet, D.U. Sauer, Separation of predominant processes in electrochemical impedance spectra of lithium-ion batteries with Nickel-Manganese-Ccobalt cathodes, J. Power Sources 425 (2019) 121–129.
[3] Y. Qi, H. Guo, L.G. Hector, A. Timmons, Threefold increase in the Young's Modulus of graphite negative electrode during lithium intercalation, J. Electrochem. Soc. 157 (5) (2010) A558–A566.
[4] N. Nitta, F. Wu, J.T. Lee, G. Yushin, Li-ion battery materials: present and future, Mater. Today 18 (5) (2015) 252–264.
[5] J.-M. Tarascon, M. Armand, Issues and challenges facing rechargeable lithium batteries, Materials for Sustainable Energy (2011) 171–179.
[6] Y.-K. Sun, S.-T. Myung, B.-C. Park, J. Prakash, I. Belharouak, K. Amine, High-energy cathode material for long-life and safe lithium batteries, Nat. Mater. 8 (4) (2009) 320.
[7] W. Zhao, J. Zheng, L. Zou, H. Jia, B. Liu, H. Wang, M.H. Engelhard, C. Wang, W. Xu, Y. Yang, et al., High voltage operation of Ni-rich NMC cathodes enabled by stable electrode/electrolyte interphases, Advanced Energy Materials (2018) 1800297.
[8] A. Boulineau, L. Simonin, J.-F. Colin, C. Bourbon, S. Patoux, First evidence of manganese–nickel segregation and densification upon cycling in Li-rich layered oxides for lithium batteries, Nano Lett. 13 (8) (2013) 3857–3863.
[9] X. Zhang, W. Jiang, A. Mauger, F. Gendron, C. Julien, et al., Minimization of the cation mixing in $Li_{1+x}(NMC)_{1-x}O_2$ as cathode material, J. Power Sources 195 (5) (2010) 1292–1301.
[10] F. Wu, J. Tian, Y. Su, J. Wang, C. Zhang, L. Bao, T. He, J. Li, S. Chen, Effect of Ni^{2+} content on lithium/nickel disorder for Ni-rich cathode materials, ACS Appl. Mater. Interfaces 7 (14) (2015) 7702–7708.
[11] O. Dolotko, A. Senyshyn, M. Mühlbauer, K. Nikolowski, H. Ehrenberg, Understanding structural changes in NMC Li-ion cells by in situ neutron diffraction, J. Power Sources 255 (2014) 197–203.
[12] K. Min, K. Kim, C. Jung, S.-W. Seo, Y.Y. Song, H.S. Lee, J. Shin, E. Cho, A comparative study of structural changes in lithium nickel cobalt manganese oxide as a function of Ni content during delithiation process, J. Power Sources 315 (2016) 111–119.
[13] H. Tsunekawa, S. Tanimoto, R. Marubayashi, M. Fujita, K. Kifune, M. Sano, Capacity fading of graphite electrodes due to the deposition of manganese ions on them in Li-ion batteries, J. Electrochem. Soc. 149 (10) (2002) A1326–A1331.
[14] J. Wandt, A. Freiberg, R. Thomas, Y. Gorlin, A. Siebel, R. Jung, H.A. Gasteiger, M. Tromp, Transition metal dissolution and deposition in Li-ion batteries investigated by operando X-ray absorption spectroscopy, J. Mater. Chem. 4 (47) (2016) 18300–18305.
[15] J.A. Gilbert, I.A. Shkrob, D.P. Abraham, Transition metal dissolution, ion migration, electrocatalytic reduction and capacity loss in lithium-ion full cells, J. Electrochem. Soc. 164 (2) (2017) A389–A399.
[16] L. Madec, L.D. Ellis, Exploring interactions between electrodes in Li $[Ni_xMn_yCo_{1-xy}]O_2$/graphite cells through electrode/electrolyte interfaces analysis, J. Electrochem. Soc. 164 (14) (2017) A3718–A3726.
[17] G.A. Elia, U. Ulissi, F. Mueller, J. Reiter, N. Tsiouvaras, Y.-K. Sun, B. Scrosati, S. Passerini, J. Hassoun, A long-life lithium ion battery with enhanced electrode/electrolyte interface by using an ionic liquid solution, Chemistry–A European Journal 22 (20) (2016) 6808–6814.
[18] Y. Qian, P. Niehoff, M. Börner, M. Grützke, X. Mönnighoff, P. Behrends, S. Nowak, M. Winter, F.M. Schappacher, Influence of electrolyte additives on the cathode electrolyte interphase (CEI) formation on $LiNi_{1/3}Mn_{1/3}Co_{1/3}O_2$ in half cells with Li metal counter electrode, J. Power Sources 329 (2016) 31–40.
[19] W. Li, A. Dolocan, P. Oh, H. Celio, S. Park, J. Cho, A. Manthiram, Dynamic behaviour of interphases and its implication on high-energy-density cathode materials in lithium-ion batteries, Nat. Commun. 8 (2017) 14589.
[20] D. Sun, Q. Wang, J. Zhou, Y. Lyu, Y. Liu, B. Guo, Forming a stable CEI layer on $LiNi_{0.5}Mn_{1.5}O_4$ cathode by the synergy effect of FEC and HDI, J. Electrochem. Soc. 165 (10) (2018) A2032–A2036.
[21] J. Choi, A. Manthiram, Comparison of the electrochemical behaviors of stoichiometric $LiNi_{1/3}Co_{1/3}Mn_{1/3}O_2$ and lithium excess $Li_{1.03}(Ni_{1/3}Co_{1/3}Mn_{1/3})_{0.97}O_2$, Electrochem. Solid State Lett. 7 (10) (2004) A365–A368.
[22] P.-C. Tsai, B. Wen, M. Wolfman, M.-J. Choe, M.S. Pan, L. Su, K. Thornton, J. Cabana, Y.-M. Chiang, Single-particle measurements of electrochemical kinetics in NMC and NCA cathodes for Li-ion batteries, Energy Environ. Sci. 11 (4) (2018) 860–871.
[23] J. Vetter, P. Novák, M.R. Wagner, C. Veit, K.-C. Möller, J. Besenhard, M. Winter, M. Wohlfahrt-Mehrens, C. Vogler, A. Hammouche, Ageing mechanisms in lithium-ion batteries, J. Power Sources 147 (1–2) (2005) 269–281.
[24] S. Bhattacharya, A.R. Riahi, A.T. Alpas, A transmission electron microscopy study of crack formation and propagation in electrochemically cycled graphite electrode in lithium-ion cells, J. Power Sources 196 (20) (2011) 8719–8727.
[25] E. Markervich, G. Salitra, M. Levi, D. Aurbach, Capacity fading of lithiated graphite electrodes studied by a combination of electroanalytical methods, Raman spectroscopy and SEM, J. Power Sources 146 (1–2) (2005) 146–150.
[26] A.J. Warnecke, Degradation Mechanisms in NMC-Based Lithium-Ion Batteries, Dissertation, Aachen, Germany, 2017.
[27] J.P. Schmidt, P. Berg, M. Schönleber, A. Weber, E. Ivers-Tiffée, The distribution of relaxation times as basis for generalized time-domain models for Li-ion batteries, J. Power Sources 221 (2013) 70–77.
[28] B. Manikandan, V. Ramar, C. Yap, P. Balaya, Investigation of physico-chemical processes in lithium-ion batteries by deconvolution of electrochemical impedance spectra, J. Power Sources 361 (2017) 300–309.
[29] H. Schichlein, A.C. Müller, M. Voigts, A. Krügel, E. Ivers-Tiffée, Deconvolution of electrochemical impedance spectra for the identification of electrode reaction mechanisms in solid oxide fuel cells, J. Appl. Electrochem. 32 (8) (2002) 875–882.
[30] J.P. Schmidt, T. Chrobak, M. Ender, J. Illig, D. Klotz, E. Ivers-Tiffée, Studies on $LiFePO_4$ as cathode material using impedance spectroscopy, J. Power Sources 196 (12) (2011) 5342–5348.
[31] H. Witzenhausen, Elektrische Batteriespeichermodelle: Modellbildung, Parameteridentifikation und Modellreduktion, Dissertation, Aachen, Germany, 2017.
[32] S. Havriliak, S. Negami, A complex plane representation of dielectric and mechanical relaxation processes in some polymers, Polymer 8 (1967) 161–210.
[33] M. Schoenleber, Kramers-Kronig Validity Test Lin-KK for Impedance Spectra, Karlsruhe Institute of Technology, Materials for Electrical and Electronic Engineering, 2017. https://www.iam.kit.edu/wet/english/Lin-KK.php.
[34] H. Witzenhausen, FittingGUI, RWTH Aachen University, Institute for Power Electronics and Electrical Drives, 2017. https://github.com/HWitz/FittingGUI.
[35] T.H. Wan, M. Saccoccio, C. Chen, F. Ciucci, Influence of the discretization methods on the distribution of relaxation times deconvolution: implementing radial basis functions with DRTtools, Electrochim. Acta 184 (2015) 483–499.
[36] J. Schmitt, A. Maheshwari, M. Heck, S. Lux, M. Vetter, Impedance change and capacity fade of lithium nickel manganese cobalt oxide-based batteries during calendar aging, J. Power Sources 353 (2017) 183–194.
[37] S.F. Schuster, T. Bach, E. Fleder, J. Müller, M. Brand, G. Sextl, A. Jossen, Nonlinear aging characteristics of lithium-ion cells under different operational conditions, Journal of Energy Storage 1 (2015) 44–53.
[38] M. Dubarry, C. Truchot, B.Y. Liaw, Cell degradation in commercial $LiFePO_4$ cells with high-power and high-energy designs, J. Power Sources 258 (2014) 408–419.
[39] M. Lewerenz, Dissection and Quantitative Description of Aging of Lithium-Ion Batteries Using Non-destructive Methods Validated by Post-mortem-analyses, Aachen, Germany, Dissertation, 2018.
[40] X. Zhou, J. Huang, Z. Pan, M. Ouyang, Impedance characterization of lithium-ion batteries aging under high-temperature cycling: importance of electrolyte-phase diffusion, J. Power Sources 426 (2019) 216–222.
[41] A. Eddahech, O. Briat, J.-M. Vinassa, Performance comparison of four lithium–ion battery technologies under calendar aging, Energy 84 (2015) 542–550.
[42] S. Zhang, M.S. Ding, K. Xu, J. Allen, T.R. Jow, Understanding solid electrolyte interface film formation on graphite electrodes, Electrochem. Solid State Lett. 4 (12) (2001) A206–A208.
[43] L. Tan, L. Zhang, Q. Sun, M. Shen, Q. Qu, H. Zheng, Capacity loss induced by lithium deposition at graphite anode for lifepo4/graphite cell cycling at different temperatures, Electrochim. Acta 111 (2013) 802–808.
[44] F.E. Hust, Physico-chemically Motivated Parameterization and Modelling of Real-Time Capable Lithium-Ion Battery Models: a Case Study on the Tesla Model S Battery, Dissertation, Aachen, Germany, 2019.
[45] T. Waldmann, M. Wilka, M. Kasper, M. Fleischhammer, M. Wohlfahrt-Mehrens, Temperature dependent ageing mechanisms in lithium-ion batteries–a post-mortem study, J. Power Sources 262 (2014) 129–135.
[46] Y. Li, M. Bettge, B. Polzin, Y. Zhu, M. Balasubramanian, D. Abraham, Understanding long-term cycling performance of $Li_{1.2}Ni_{0.15}Mn_{0.55}Co_{0.1}O_2$-graphite lithium-ion cells, J. Electrochem. Soc. 160 (5) (2013) A3006–A3019.